scientific reports

Check for updates

OPEN

Probabilistic nested model selection in pharmacokinetic analysis of DCE-MRI data in animal model of cerebral tumor

Hassan Bagher-Ebadian[1,2,3,4 ✉], Stephen L. Brown[1,2,4], Mohammad M. Ghassemi[5], Prabhu C. Acharya[3], Indrin J. Chetty[3,6], Benjamin Movsas[1,2], James R. Ewing[2,3,7] & Kundan Thind[1,2,4]

Best current practice in the analysis of dynamic contrast enhanced (DCE)-MRI is to employ a voxel-by-voxel model selection from a hierarchy of nested models. This nested model selection (NMS) assumes that the observed time-trace of contrast-agent (CA) concentration within a voxel, corresponds to a singular physiologically nested model. However, admixtures of different models may exist within a voxel's CA time-trace. This study introduces an unsupervised feature engineering technique (Kohonen-Self-Organizing-Map (K-SOM)) to estimate the voxel-wise probability of each nested model. Sixty-six immune-compromised-RNU rats were implanted with human U-251 N cancer cells, and DCE-MRI data were acquired from all the rat brains. The time-trace of change in the longitudinal-relaxivity (ΔR_1) for all animals' brain voxels was calculated. DCE-MRI pharmacokinetic (PK) analysis was performed using NMS to estimate three model regions: Model-1: normal vasculature without leakage, Model-2: tumor tissues with leakage without back-flux to the vasculature, Model-3: tumor vessels with leakage and back-flux. Approximately two hundred thirty thousand (229,314) normalized ΔR_1 profiles of animals' brain voxels along with their NMS results were used to build a K-SOM (topology-size: 8×8, with competitive-learning algorithm) and probability map of each model. K-fold nested-cross-validation (NCV, k = 10) was used to evaluate the performance of the K-SOM probabilistic-NMS (PNMS) technique against the NMS technique. The K-SOM PNMS's estimation for the leaky tumor regions were strongly similar (Dice-Similarity-Coefficient, DSC = 0.774 [CI: 0.731–0.823], and 0.866 [CI: 0.828–0.912] for Models 2 and 3, respectively) to their respective NMS regions. The mean-percent-differences (MPDs, NCV, k = 10) for the estimated permeability parameters by the two techniques were: -28%, +18%, and +24%, for v_p, K^{trans}, and v_e, respectively. The KSOM-PNMS technique produced microvasculature parameters and NMS regions less impacted by the arterial-input-function dispersion effect. This study introduces an unsupervised model-averaging technique (K-SOM) to estimate the contribution of different nested-models in PK analysis and provides a faster estimate of permeability parameters.

In the pharmacokinetic (PK) analysis of brain dynamic contrast-enhanced magnetic resonance imaging (DCE-MRI) data, the principle of parsimony serves as an accepted heuristic[1]. Under the constraint of parsimony, the simplest physiologically meaningful model that sufficiently represents the temporal variation of DCE-MRI data is the best choice for producing stable estimates of model parameters. Parsimonious PK parameters effectively summarize the pathophysiological behavior of the underlying brain tissue by balancing variance and bias in parametric estimates[2,3]. Our research group has introduced a nested model selection (NMS) technique for DCE-

[1]Department of Radiation Oncology, Henry Ford Hospital, Detroit, USA. [2]Department of Radiology, Michigan State University, East Lansing, USA. [3]Department of Physics, Oakland University, Rochester, USA. [4]Department of Oncology, School of Medicine, Wayne State University, Detroit, USA. [5]Department of Computer Science and Engineering, Michigan State University, East Lansing, USA. [6]Department of Radiation Oncology, Cedars-Sinai Medical Center, Los Angles, USA. [7]Department of Neurology, Henry Ford Hospital, Detroit, USA. ✉email: hbagher1@hfhs.org

MRI analysis in rat and human brains that utilizes an extended Patlak graphical method[2,3] as the highest-order model. This NMS approach enhances the stability of dynamic contrast enhanced (DCE) MRI data processing[2,3]. However, it relies on the strong assumption that each voxel's measured time trace of contrast agent (CA) concentration corresponds to a single physiologically nested model. This assumption may produce systematic errors in the parametric estimates; for a given voxel's time trace of CA concentration, combinations of different NM's with different contribution levels likely exist.

In this study, we introduce an unsupervised probabilistic nested model selection (PNMS) method based on the model averaging concept for DCE-MRI PK analysis of animal model of cerebral tumor using a Kohonen-Self-Organizing Map (K-SOM) technique. The proposed model is constructed by the concentration-time trace of MR relaxivity change (ΔR_1) estimated from DCE-MRI information of animal model of brain tumor to perform a PNMS based on the nested model selection results. The PNMS can rank and estimate the uncertainty and probability of different nested models as well as their contribution levels in a given voxel to address the voxel-wise 'model averaging' concept that results in a faster estimation of PK parameters.

Methods

Imaging and animal population

Using previously published methods[4], sixty-six athymic RNU rats (10–12 weeks old and 200–230 g, Charles River Laboratories, Wilmington, MA), implanted with human U-251 N cells. U-251 N cells were maintained in Dulbecco's Minimum Essential Media (DMEM) with 10% fetal bovine serum (FBS) and 1% streptomycin and penicillin. Cell cultures were passaged once a week and not more than 4 times. The concentrations of human U-251 N cells were 5×10^9 cells per mL, which were loaded into a 10 μL Hamilton syringe (Model 701, Hamilton Co., Reno, NV) before implantation. Rat brains were implanted with human U-251 N cancer cells to form orthotopic gliomas. A DCE-MRI study was performed using a Dual-Echo Gradient-Echo – DGE pulse sequence (400 acquisitions, with TE/TR = 1.55/24.19 [ms]), tail-vein with contrast injection of Magnevist with 0.25 mmol/kg at undiluted concentration without ~ 60 s after the start of the experiment. Two T_1 mapping sequences (Look-Locker Inversion Recovery) were also acquired from all rat brains[5] before and after the DCE-MRI experiment. All studies used a Varian/Magnex (Santa Clara, CA), 7 Tesla, 20 cm bore magnet with a Bruker console running Paravision 6.0 software. Gradient maximum strengths and rise times were 250 mT/m and 120 μs. Following published procedures[2,6], all two-dimensional MRI image sets were acquired with a 32×32 mm^2 field of view (FOV). Transmitter and receiver coils included a Bruker Quadrature Birdcage (transmit) and 4-channel phased-array surface coil receiver (Rapid MR International, Columbus, OH).

Ethical approval

All experimental and imaging procedures were conducted at our institution under an protocol approved by the Institutional Animal Care and Use Committee (IACUC) of Henry Ford Health (number 1509) and was performed and reported in compliance with the ARRIVE guidelines[7–9]. Also, all methods were performed in accordance with the relevant guidelines and regulations[7–9]. All animals were anesthetized before and during the MRI experiment using Isoflurane. After all experimental studies were completed, rats were euthanized with an overdose of isofluorane, followed by transcardial perfusion and fixation.

Calculation of contrast agent concentration from DCE-MRI data

We assume that the gadolinium contrast agent (CA) concentration, [Gd], is proportional to the change in the longitudinal relaxation rate (R_1) after CA administration: $[Gd] = C(t) \sim \Delta R_1(t)$, where $R_1 = 1/T_1$ and T_1 is the longitudinal relaxation time. We assume that longitudinal relaxivity for Gd is constant across tissues. Dual Gradient Echo (DGE) imaging allows for the computation of T_1 and T_2^* as approximately pure and independent components[10,11]. This is essential for the estimation of CA concentration based on ΔR_1 and ΔR_2^*. We previously introduced and developed methods for estimating the ΔR_1 signal (~ CA concentration) from the DGE pule sequence. As previously noted[2], this method introduces equations to describe the measured T_1-weighted intensities of the first and second echo signals and their relationship to the longitudinal and transverse relaxation times (T_1, T_2^*), repetition time (T_R), echo time (T_E), flip angle (θ), and equilibrium longitudinal magnetization (M_0). T_2^* includes the effects of both static dephasing and irreversible dephasing. In this study, the voxel-wise profiles of the CA concentration map, $\Delta R_1(t)$, were directly estimated from the DCE-MRI experiment, and the pre and post T_1 maps estimated by the pre- and post-DCE T_1 pulse sequences (T One by Multiple Read Out Pulses, TOMROP/Look-locker[12]). The time trace of change in the longitudinal relaxation time, ΔR_1 in all the voxels of the animal's brain, corresponding and proportional to the time trace of contrast agent concentration, for 66 rat brains' DCE-MRI studies were calculated[3]. Dual Gradient Echo (DGE) imaging allows for the computation of T_1 and T_2^* as approximately pure and independent components[10,11]. At 7T field strength, this is essential for an unbiased estimation of CA concentration. We employed a Look-Locker inversion recovery sequence to make pre-contrast and post-DGE voxel-by-voxel estimates of tissue T1. After calculating[10,11] the pure and independent components (T_1 and T_2^*) of the DGE signals, we used voxel-wise T_1 (longitudinal relaxation time) values of the signals calculated from pre and post injection TOMROP pulse sequences to calculate the change in the longitudinal relaxation rate (ΔR_1) at time points after contrast agent (CA) administration, and used this, along with a tissue-normalized Arterial Input Function, as estimates for contrast agent concentration-time curves.

Post-processing and conventional nested model selection in PK analysis

Post-processing and pharmacokinetic compartmental analyses of DCE-MRI data were carried out following published methods[2,3]. We used a nested model selection (NMS)[2,3,13] paradigm based on Patlak and extended-Patlak graphical methods[14,15]. As illustrated in subfigure 1 A, we have shown[2,3] that three physiologically nested models can be derived from the standard model to describe possible physiological conditions of underlying
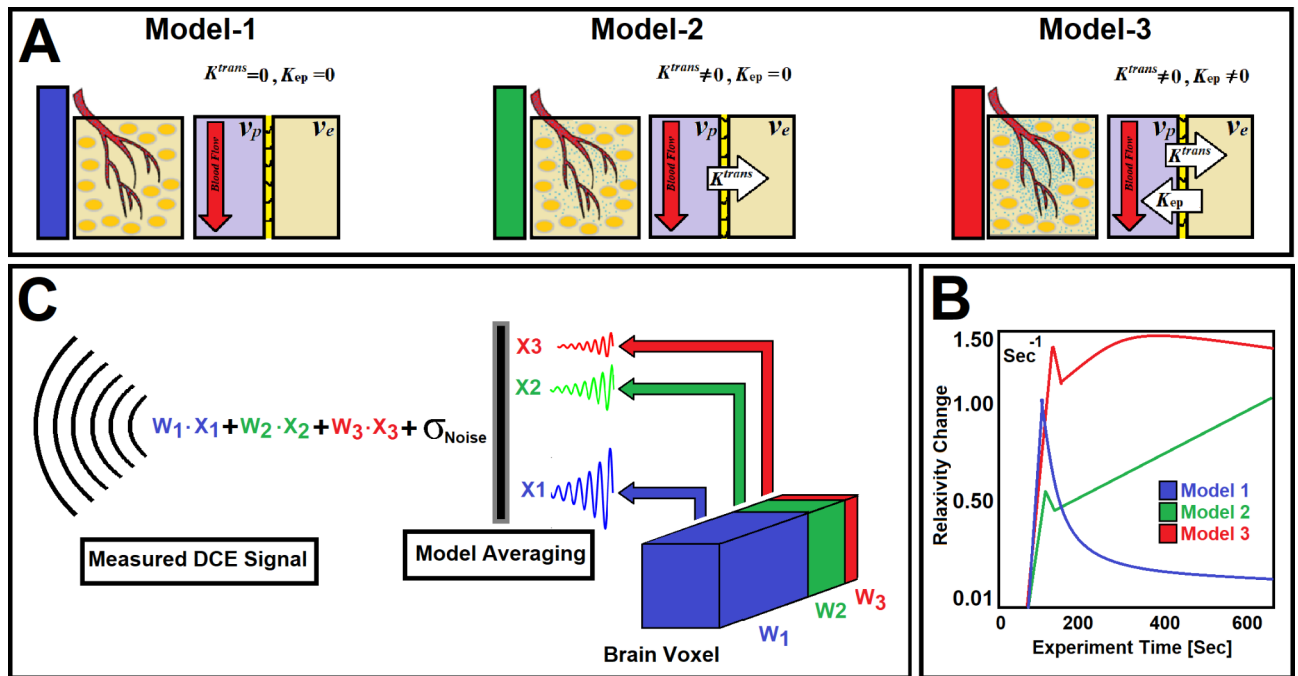
Fig. 1. (**A**) illustrates three physiologically nested models, their vascular and extra-cellular-extra vascular compartments, and their estimable vascular parameters. (**B**) shows typical time-traces of the CA concentration computed for the three nested models according to the observation equations (Eqs. 1–3) for typical permeability parameters. (**C**) demonstrates the concept of the model averaging technique for estimation of the probabilistic nested model selection from the conventional NMS results for a typical voxel.

tissue pathology[2,3]. We have generated a series of stable processing pipelines accordingly, to produce vascular parametric maps based on the NMS technique[2,3]. As shown in subfigure 1 A, the NMS method[2,3] was used to generate maps of brain regions labeled with the number of permeability parameters used to describe the data[2]: *(a)* Model 1 region: normal vasculature with no leakage, the only parameter estimated is plasma volume, v_p; *(b)* Model 2 region: tumor tissues with CA leakage without measurable back-flux to the vasculature, in which case v_p and, K^{trans} can be estimated; or *(c)* Model 3 region: tumor vessels with CA leakage and measurable back-flux and, thus, v_p, K^{trans}, and k_{ep}, or extracellular extra-vascular volume, v_e (ratio of K^{trans} and K_{ep}) can be estimated. Three model equations representing the three physiologically nested models were constructed as follows (Eqs. 1–3) and used for the conventional PK NMS analysis:

$$C_{tissue}(t) = [v_p C_{AIF}(t)] \tag{1}$$

$$C_{tissue}(t) = [v_p C_{AIF}(t) + K^{trans} \int_0^t C_{AIF}(\lambda)\, d\lambda] \tag{2}$$

$$C_{tissue}(t) = [v_p C_{AIF}(t) + K^{trans} \int_0^t C_{AIF}(\lambda)\, e^{-K_{ep}(t-\lambda)} d\lambda] \tag{3}$$

Where $C_{AIF}(t)$ and $C_{tissue}(t)$ refer to the contrast agent (CA) concentration measured from plasma (or arterial input function, AIF) and tissue of interest in the brain, respectively. Hematocrit ratio (H_{ct}) was not included in the equations. The assumption is that the CA is excluded from the erythrocytes of blood, and that the change in R_1 is proportional to the concentration of CA in plasma. Since we are estimating plasma volume, there's no correction warranted for H_{ct}. To allow the spin system to reach a true equilibrium after the start of the highly saturated DCE-MR imaging, the first 20 timepoints of the pre-injection part of the signals were excluded from the analysis (about 30 s). For each observation equation (Eqs. 1–3), the voxel-by-voxel time trace of ΔR1(t) in rat brain was used to estimate its PK parameters. At image 15 (corresponds to ~ 23 s after the start of the DCE experiment) of the DGE sequence, a bolus injection of the CA (Magnevist; Bayer HealthCare LLC, Wayne, NJ, 0.25 mmol/kg at undiluted concentration, no flush) was performed. The group averaged radiological trace was normalized to the time trace of CA concentration in the animal's normal caudate putamen[16], with the assumption that plasma volume fraction in caudate putamen is 1%. Then, the normalized radiological AIF was used as CA concentration measured from plasma.

In the NMS analysis[3], the F-statistic generated in three models (1, 2 and 3) can be directly compared to its reduced model alternative, thus allowing an unambiguous selection of model and model parameters best supported by the data. After converting the data into a time trace of the change from baseline in the longitudinal

relaxation rate, ΔR_1 ($R_1 = 1/T_1$), it was used as a measure of the change of CA tissue concentration with time. Then, for each voxel, the three nested models (1, 2 and 3) were fitted to the concentration-time curve, ΔR_1, and the F-statistics comparing Model 1 to Model 2 (leakage without vascular reabsorption), and Model 2 to Model 3 (leakage with reabsorption) were calculated. Each F-statistic was thresholded at the 95% confidence level and used as a statistical criterion to compare each of models to their possible reduced versions and to perform the nested model selection. In the F-test, the null hypothesis is that the two samples of sum-squared residuals were drawn from the same pool. The failure of this hypothesis leads to acceptance of the higher-order model. The probability associated with the F-test (the p-value) is that of a Type I error, e.g., the probability of accepting Model 3 when the underlying truth is that of Model 2. In comparing model alternatives voxel-by-voxel, the confidence level (CL) was set at 95% for the main analysis. Finally, all the rat brains' ΔR_1 profiles ($n = 229,314$) were labeled (149668, 60268, and 19378 profiles for Models 1, 2 and 3, respectively) according to their selected models at 95% CL.

Model development and validation

A total of 229,314 normalized profiles (149668, 60268, and 19378 profiles for Models 1, 2 and 3, respectively) were extracted from the rat brains' voxels and used to construct and validate the unsupervised K-SOM method[17,18].

An unsupervised machine learning technique, A K-SOM[17,18] or self-organizing feature map, was used to produce a low-dimensional representation of higher dimensional data set with complex structures while preserving the topological structure of the data. During the K-SOM analysis, a competitive learning algorithm[19–21] along with Best Matching Unit (BMU) strategy were employed to identify the "winner" nodes/neurons for an 8×8 topology. The cover steps for initial covering of the input space for ordering the phase steps of the K-SOM was set to 100. The K-SOM's architecture was hexagonal with an initial neighborhood size of three, and the maximum epoch was set to 250 epochs for batch training mode. A BMU-based hit map was generated for the CA concentration profiles within the animal brains. The model choice labels for all three models (at the Confidence Level of CL = 95%) estimated from the conventional PK-NMS analyses for all profiles were used as the source of truth for the conventional nested models (with high Confidence Level: 95%) to calculate the tagged BMUs on the K-SOM topology space. The hit maps and their corresponding labels were used to estimate the three K-SOM probability and iso-probability maps for the three different model choices.

Dice Similarity Coefficients (DSCs)[22] for different model regions generated by the conventional NMS analysis and the K-SOM probabilistic NMS (at NMS probabilities of 50%) were used to evaluate the performance of the trained K-SOM and the conventional NMS on DCE-MRI data. The calculated DSCs compared the similarity of the model regions estimated by the PNMS technique against the physiological state identified by the conventional NMS method.

To investigate and validate the performance of the constructed K-SOM to perform the probabilistic NMS on DCE-MRI data for the three physiologically nested models, a k-fold (k = 10) Nested Cross Validation (NCV) analysis[23] was performed. The full dataset for all the three models was randomly permuted (using Random Permutation Sampling, RPS[24]) and split into 10 non-overlapping folds[25] (ratio for training/test: 0.66/0.34, 44/22 [26]). Two independent loops were defined as outer and inner loops. In the outer loop, for each epoch, the data was split into two folds (training + validation fold, and a test fold), and for the inner loop, only the validation + training fold was used to construct a series of K-SOMs. Then, for each iteration, an unsupervised K-SOM was constructed in the inner loop using the training cohorts. The trained K-SOM constructed in each fold of the inner loop was used as the PNMS predictor of the test cohorts of its respective fold in the outer loop. This process was repeated 10 times (k = 10) and at each repetition, an independent test set was withheld for the estimation of the performance of the constructed K-SOM PNMS model of the inner loop for different nested models and their respective permeability parameters.

For each iteration of k-fold NCV, to calculate the probabilities of the three models on the K-SOM's feature space, all the normalized ΔR_1 profiles (annotated from the conventional PK-NMS) of the training cohort, were used to construct the K-SOM's hit map. For each K-SOM's neuron (located at (n, m) within the network topology, $n = 1,2,0.8$ and $m = 1,2,0.8$), the probability of that neuron being the winner neuron for each model j,

was calculated as follows: $P_j(m, n) = \frac{1}{(\sum_1^8 n).(\sum_1^8 m)} \left(\frac{K_j(m,n)}{K_1(m,n) + K_2(m,n) + K_3(m,n)} \right)$. Where the index j refers to different nested models (j = 1,2,3) and $K_j(m, n)$ refers to the number/frequency of the best matching unit (BMU) or number of time the neuron located at n, and m wins for model j.

In each iteration, the model 1 region estimated by the PNMS at 50% threshold was used to mask-out the whole brain to identify the two model regions (Models 2 and 3) of the rat brains. Then, two DSCs were calculated and averaged (over the 10 folds) for the model 2 and 3 regions estimated by the conventional NMS (at the Confidence Level of 95%) and K-SOM PNMS techniques. We thresholded the PNMS maps at 50% (columns 3 and 4 in Fig. 5, for Models 2 and 3, respectively) and used the generated masks for masking out the PNMS and NMS maps for the computation of Models 2 and 3's DSCs. Finally, for different model regions, three permeability parameters were estimated and averaged over the 10-fold nested cross validation for the two techniques and their mean percent differences (MPD) were calculated. The voxel-wise permeability parameters, $v_p(x, y, z)$, $K^{trans}(x, y, z)$, and $v_e(x, y, z)$, for the K-SOM PNMS technique were calculated as follows:

$$v_p(x,y,z) = \frac{P_1(x,y,z).v_p^{(M1)}(x,y,z) + P_2(x,y,z).v_p^{(M2)}(x,y,z) + P_3(x,y,z).v_p^{(M3)}(x,y,z)}{P_1(x,y,z) + P_2(x,y,z) + P_3(x,y,z)} \quad (4)$$

$$K^{trans}(x,y,z) = \frac{P_2(x,y,z).K^{trans\,(M2)}(x,y,z) + P_3(x,y,z).K^{trans\,(M3)}(x,y,z)}{P_2(x,y,z) + P_3(x,y,z)} \quad (5)$$

$$v_e\left(x, y, z\right) = \frac{K^{trans}\left(x, y, z\right)}{K_{ep}^{(M3)}\left(x, y, z\right)} \quad (6)$$

where $P_1(x, y, z)$, $P_2(x, y, z)$, and $P_3(x, y, z)$ refers to the voxel-wise probabilities for the three nested models: models 1, 2, and 3, respectively. The $v_p^1(x, y, z)$, $v_p^2(x, y, z)$, and $v_p^3(x, y, z)$ in Eq. 1 refers to the estimated voxel-wise plasma volumes for models 1, 2, and 3, using the conventional NMS technique. The $K^{trans\,(M2)}(x, y, z)$, and $K^{trans\,(M3)}(x, y, z)$ in Eq. 2 refers to the voxel-wise forward transfer constants estimated for the nested models 1 and 2 using the conventional NMS technique. The $K_{ep}^3(x, y, z)$ in Eq. 3 refers to the voxel-wise reverse transfer constant for model 3 using the conventional NMS technique.

Results

Subfigure 1 A illustrates three physiologically nested models, their vascular and extra-cellular extra-vascular compartments, and their estimable vascular parameters according to the concept of conventional NMS technique. Subfigure 1B shows graphs of typical time-traces of the CA concentration (ΔR_1) computed for the three nested models according to the observation equations (Eqs. 1–3) for typical permeability parameters. Subfigure 1 C demonstrates the concept of the model averaging technique for estimation of the probabilistic nested model selection from the conventional NMS results for a typical voxel. Subfigure 2 A and 2B illustrate the first and second echo of the DCE-DGE for a slice of rat brain about 8 min after the tail vein administration of CA. Subfigure 2 C-F demonstrates the model choice map and its corresponding permeability parameter maps (v_p, K^{trans}, and v_e) calculated by the conventional NMS technique for the same slice of rat brain. Subfigure 3 A illustrates the normalized K-SOM hit map (BMU) constructed from 66 rat brains' voxels. Subfigure 3B demonstrates the topology space of the trained K-SOM network for the three nested model probabilities on the feature space. Subfigures 3 C to 3 F show the magnified versions (zoomed by factor of 4 for a better visualization) of the K-SOM feature space probabilities for the nested models 1, 2, 3, and their fused map (coded in RGB colors) respectively. Subfigure 4 A, 4 C, and 4E illustrates the trained K-SOM probability feature spaces for different nested models with their masked-out regions (estimated at the 50% probability threshold for each model, identified by dark neurons) for the three nested models. SubFig. 4B and D, and 4 F demonstrate the normalized $\Delta R1$ averaged over the typical rat brain's regions corresponding to the selected neurons/nodes (dark neurons) on the K-SOM probability space for Models 1, 2, and 3, respectively. The K-SOM based PNMS and conventional NMS analyses results for six slices of different rat brains are shown in Fig. 5. The six columns (from left to right) of Fig. 5 demonstrate the K-SOM normalized hit map (BMU), K-SOM probability maps for the three models (Model 1, 2, and 3), K-SOM fused probability maps (coded in RGB colors) for the three nested models, and the conventional NMS map (at 95% Confidence Level), respectively.

Table 1 shows the average permeability parameters for the combined/fused model regions (model regions 1, 2 and 3 were fused for the measurement of plasma volume: v_p1, v_p2, and v_p3, model regions 2 and 3 were fused and used for the measurement of K^{trans}: $K^{trans}2$ and $K^{trans}3$, and model 3 region was used for the measurement
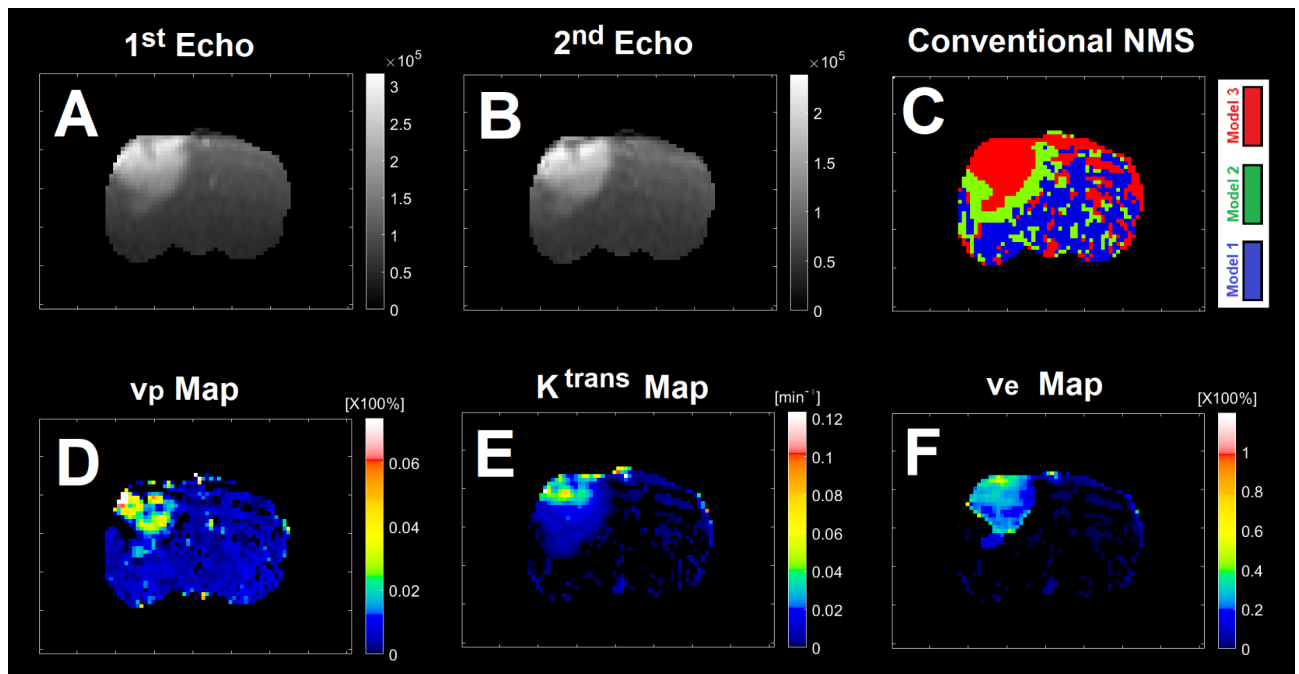

Fig. 2. (**A**) and (**B**) illustrate the first and second echo of the DCE-DGE for a slice of rat brain about 8 min after the tail vein administration of CA. (**C**)-(**F**) demonstrate the model choice map and its corresponding permeability parameter maps (v_p, K^{trans}, and v_e maps) for the same slice of rat brain.
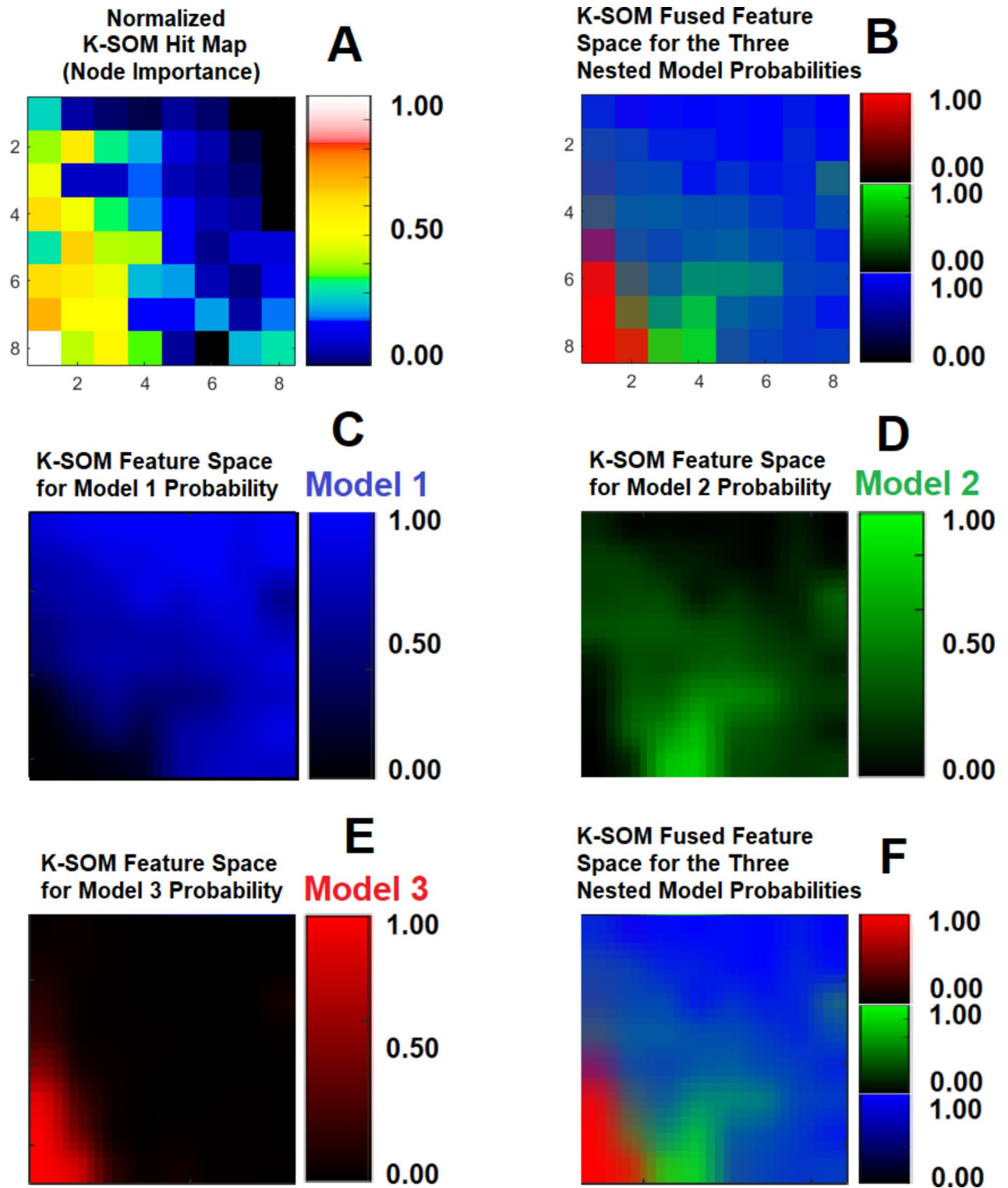
Fig. 3. (**A**) illustrates the normalized K-SOM hit map constructed from 66 rat brain's voxels. (**B**) demonstrates the topology of the trained K-SOM feature space for the three nested model probabilities. (**C**) to (**F**) show the magnified versions (for better visualization) of the K-SOM feature space probabilities for Models 1, 2, 3, and their fused map respectively.

of v_e) estimated by the conventional NMS for the k-fold NCV (k = 10). Different model regions estimated by the NMS were fused and used to measure the permeability parameters estimated by the two techniques, NMS and PNMS. The last column of the table shows the mean percent differences (100x[PNMS estimate-NMS estimate]/ NMS estimate]) of the PNMS's estimates compared to their baseline values (NMS). The average Dice Similarity
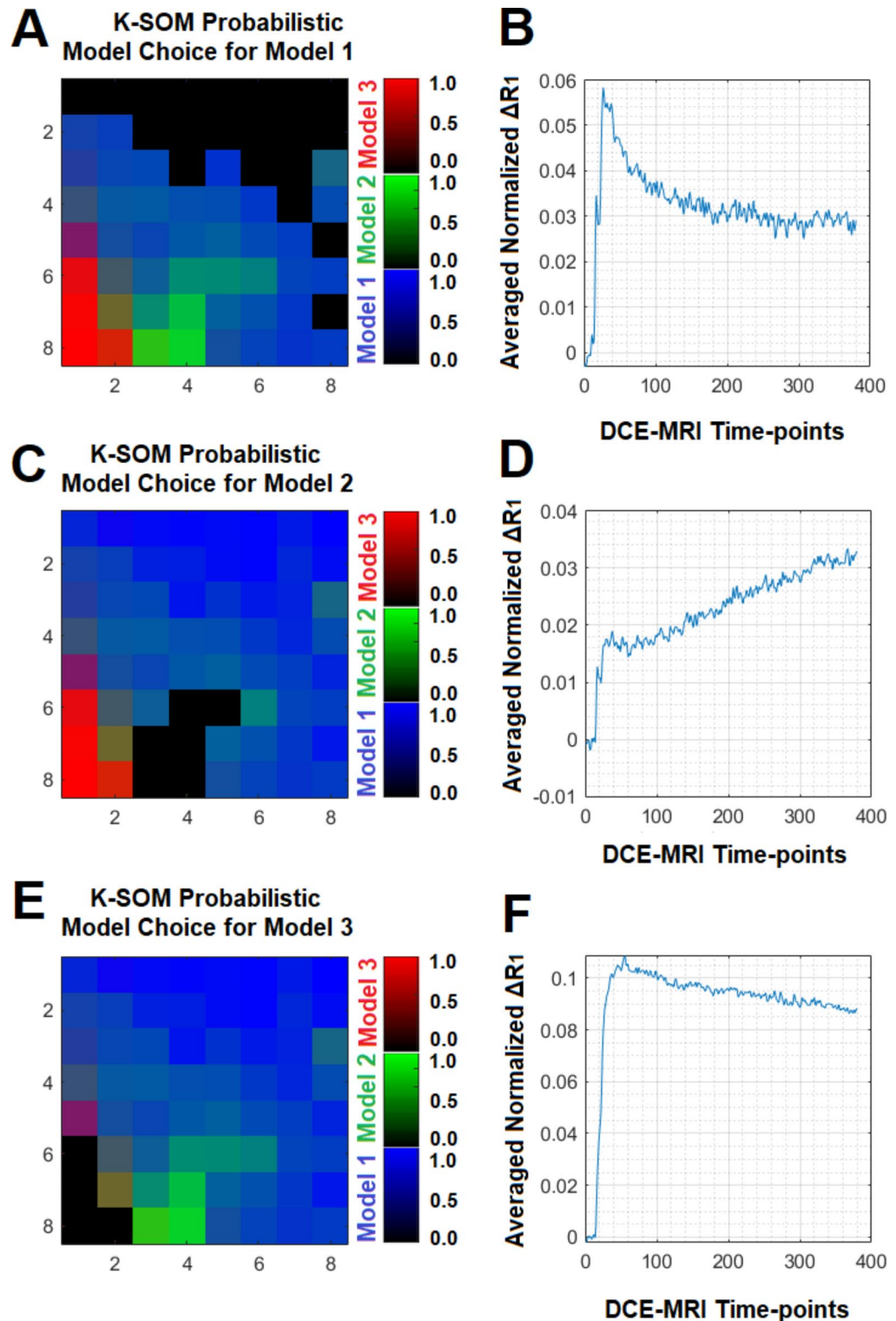
Fig. 4. (**A**), (**C**), and (**E**) illustrate the trained K-SOM probability feature spaces for the three nested models with their masked-out regions (estimated at the 50% probability threshold for each model, dark neurons) for the three nested models. (**B**), (**D**), and (**F**) demonstrate the normalized ΔR_1 averaged over the typical rat brain's regions corresponding to the selected neurons/nodes (dark neurons) on the K-SOM probability space for Models 1, 2, and 3, respectively.
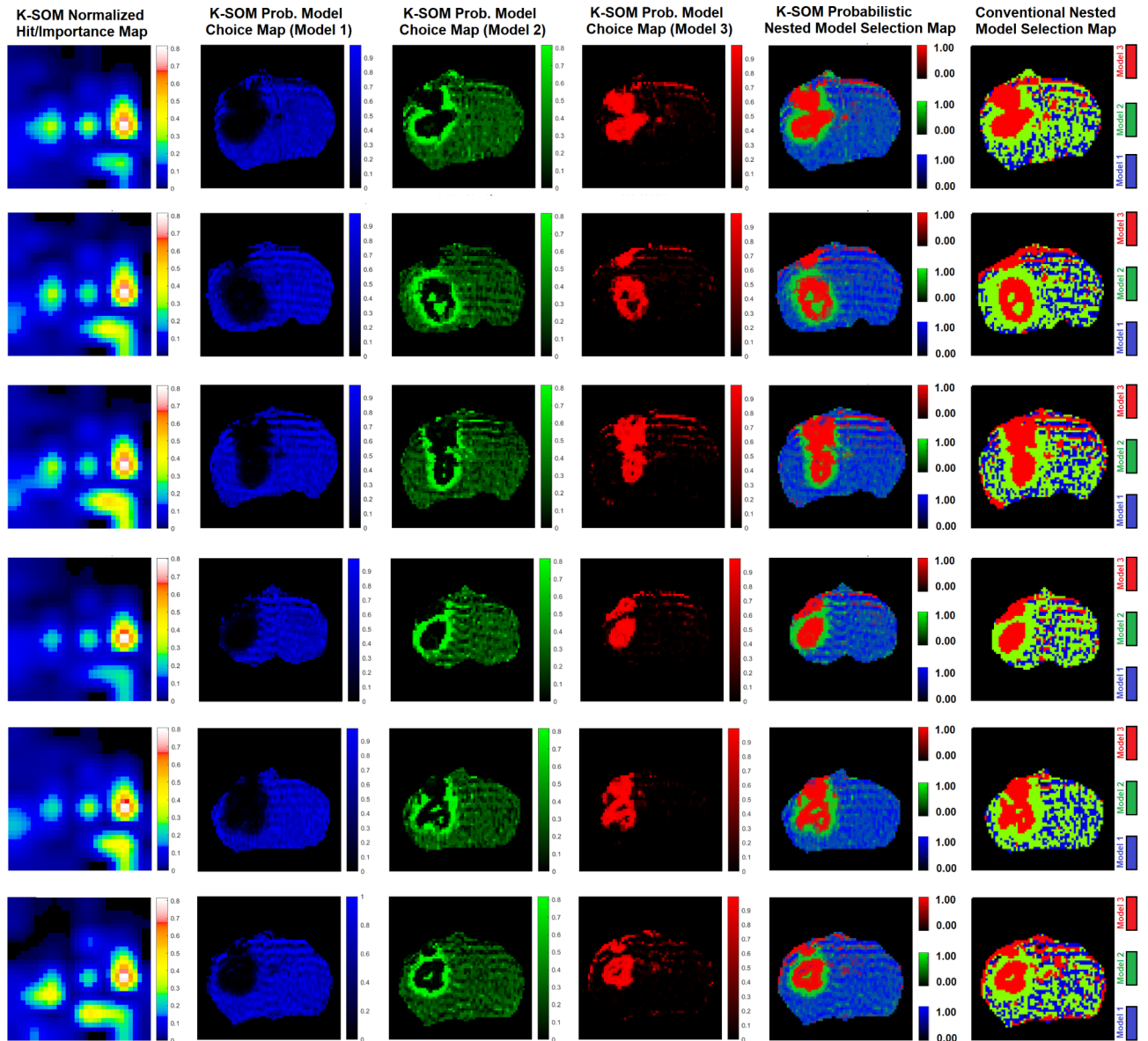
Fig. 5. The K-SOM based PNMS and conventional NMS analysis results for six slices of different rat brains are shown in this figure. The six columns (from left to right) of this figure demonstrate the K-SOM normalized hit map, K-SOM probability map for Model 1, K-SOM probability map for Model 2, K-SOM probability map for Model 3, K-SOM fused probability maps for all three models, and the conventional NMS map (at 95% Confidence Level), respectively.

	Conventional NMS			Probabilistic NMS			
	Mean	(CI-LB)	(CI-UB)	Mean	(CI-LB)	(CI-UB)	MPD [%]
Plasma Volume [%]	2.134	1.942	2.369	1.537	1.429	1.629	−28.004
Forward Volumetric Transfer Constant [1/min]	0.140	0.131	0.169	0.165	0.153	0.175	18.157
Extra Cellular Extra Vascular Volume [%]	13.649	12.284	15.287	16.949	15.424	18.136	24.179

Table 1. The average permeability parameters for the combined/fused model regions(model regions 1, 2 and 3 were fused for the measurement of plasma volume: v_p1, v_p2, and v_p3,model regions 2 and 3 were fused and used for the measurement of K^{trans}: $K^{trans}2$ and $K^{trans}3$, andmodel 3 region was used for the measurement of v_e) estimated by the conventional NMS for the kfoldNCV (k=10). Different model regions estimated by the NMS were fused and used to measurethe permeability parameters estimated by the two techniques, NMS and PNMS. The last column ofthe table shows the mean percent differences (100x[PNMS estimate-NMS estimate]/NMS estimate])of the PNMS's estimates compared to their baseline values (NMS).

Coefficients (NCV, k = 10 folds) for the leaky tissues were 0.774 [CI: 0.731–0.823], and 0.866 [CI: 0.828–0.912] for Models 2 and 3, respectively.

The average plasma volumes (NCV, k = 10) estimated by the conventional NMS and PNMS techniques were: 2.134% [CI: 1.942%, 2.369%], and 1.573% [CI: 1.429%, 1.629%], respectively. The MPD for the plasma volume was − 28.004%. The average forward volumetric transfer constant (NCV, k = 10) estimated by the conventional NMS and PNMS techniques were: 0.140 min^{-1} [CI: 0.131 min^{-1}, 0.169 min^{-1}], and 0.165 min^{-1} [CI: 0.153 min^{-1}, 0.175 min^{-1}], respectively. The MPD for the forward volumetric transfer constant was + 18.157%. The average interstitial space (NCV, k = 10) estimated by the conventional NMS and PNMS techniques were: 13.649% [CI: 12.282%, 15.287%], and 16.949% [CI: 15.424%, 18.136%], respectively. The MPD for the interstitial space was + 24.179%.

Discussion

The K-SOM analysis technique used in this study preserved and mapped the dynamic characteristics of model-based ΔR_1 information at different time points to a feature space, and also correspondingly compared the information of different time points during the mapping process using a competitive learning approach[19–21]. The K-SOM technique is an unsupervised learning method which enables detection and preservation of the topological relationship of the training dataset based on the information similarity. The main goal of the study was to evaluate and compare the voxel-wise pathophysiological information content of the DCE-MRI information, such as distribution of the different NM information, their similarities, uncertainty levels, and model diffusivity on the feature space to perform probabilistic model selection of PK data from rat brain tumors.

We investigated the feasibility of using a K-SOM technique to perform probabilistic *model averaging* on the DCE-MRI information profiles that are directly associated with tissue response (ΔR_1) compared to its conventional model selection technique to calculate the probability of different pharmacokinetic-based pathophysiological states of tissues according to the nested model selection theory.

In this study, recruitment of such an unsupervised mapping revealed different degrees of similarities and associations[17,18] among model-based dynamic information extracted from tumor and surrounding normal tissues with their respective pathophysiological states. The K-SOM probabilistic NMS concept proposed in this study allows for a selection of an optimal PK nested model, weighted with a similarity-based model information using the *'model averaging'* concept that produces a less biased estimate of permeability parameters best fitted to the DCE-MRI information[2,3]. Once constructed, the K-SOM-based PNMS (works based on the model averaging concept) in this study results in faster characterization of tumor physiology, microvasculature and microenvironmental parameters.

As shown in subfigure 3B, there are three dominant clusters on the K-SOM feature space (dark blue, dark green, and dark red) associated with the three conventional nested models. The K-SOM's neurons on the feature space with lighter colors and mixture of the shades of the three main colors (blue, green, and red) in adjacent to these dominant clusters are responsible for characterization of the voxels' temporal information that may contain more than one single physiologically nested model with a higher degree of vasculature heterogeneity. These voxels may contain a combination of normal and leaky vasculatures.

We assumed that the change in the longitudinal relaxation rate (R_1) after CA administration is proportional to the contrast agent (CA) concentration,: $[Gd] = C(t) \sim \Delta R_1(t)$, where $R_1 = 1/T_1$ and T_1 is the longitudinal relaxation time. Indeed, this assumption is well supported in most DCE-MRI studies because they are conducted under the conditions of rapid repetition time and Ernst tip-angle adjusted for a mean decrease in R_1. Under these conditions, studies in multicompartmental systems demonstrate little effect of water exchange mechanisms[26,27].

We examined the information content of the relaxivity change (ΔR_1) measured from a rat brain's voxel using an unsupervised K-SOM algorithm[17,18,28,29] to estimate the probability of the existence of different nested models within that voxel. The time traces of relaxivity change (ΔR_1) were channelled into three dominant models with high certainties (CL = 95%) using the conventional NMS technique and then projected on a two-dimensional topology space to reveal any potential non-linearities, similarities, and dissimilarities of the spatiotemporal structures of the ΔR_1 profiles in the form of clusters on the K-SOM's feature space. The notable characteristic of K-SOM method is that the detailed structures of input vectors (ΔR_1) that are close, and similar in high dimensional space are mapped to nearby nodes in its topology space. It is in essence, an unsupervised method for data dimensionality reduction and grouping the information, as it maps high-dimension inputs to a low dimensional discretized representation while conserving the underlying structures of its input space[17,18,28,29]. This generated distinct clusters with different levels of scattered fragments of ΔR_1 information without any supervision on the K-SOM's feature space. The blue, green, and red zones on the fused K-SOM's topology maps (see subfigure 3B) correspond to the models 1, 2, and 3 (estimated from the conventional NMS PK analysis with CL = 95%), respectively. The three dominant clusters in this figure strongly confirms the value and discriminant power of the ΔR_1 information for revelation and capture of the nested models' features for characterization of tumor heterogeneity and microvascular characteristics according to the conventional NMS concept. As shown in Fig. 4, the three dominant clusters associated with the three conventional nested model regions on the K-SOM's feature space produced three average ΔR_1 profiles (subFig. 4B and D, and 4 F) that are strongly in agreement with their respective graph of ΔR_1 profiles (see subfigure 1B) generated by the Eqs. 1–3.

As shown in Fig. 5, the K-SOM PNMS has produced stable maps of nested model regions with smooth transitions on their borders. The Model-1 regions (corresponding to non-leaky normal tissues) estimated by the K-SOM PNMS technique are less impacted by the dispersion effects due to the arterial input function and magnetic field gradient. This leads to a lower mis-classification for Model-1 and 2 regions. This is because the K-SOM efficiently captures the detailed characteristics of the ΔR_1 profiles and their contribution levels within the normal tissues' voxels.

The results of this study confirm that the K-SOM PNMS technique can efficiently generate probabilistic nested model maps with less-biased estimates of their respective permeability parameters compared to the conventional NMS technique. Since the K-SOM was trained with the tissue response (ΔR_1) information, this will preserve the properties or the potential pathophysiological structures of the DCE MRI data that are similar across rat and human brains for more robust modeling. Since the physiological properties of brain tissue are mostly constant across species and pathologies[30–32], the associations of tissue response information with brain tissue physiology (NMS information) revealed in this study can be expected to reliably scale and translate to human Glioblastoma (GBM) to estimate the physiological properties of solid tumors (such as glioblastoma, GBM) and soft surrounding normal tissues in embedded tumors of humans.

The average DSC values for the two models (DSC = 0.774 [CI: 0.731–0.823], and 0.866 [CI: 0.828–0.912] for Models 2 and 3, respectively) along with permeability parameters evaluated and measured from the k-fold NCV (k = 10) technique strongly confirms the convergence between the two methods (conventional and probabilistic NMS techniques) at higher level of certainties (NMS at CL = 95% and PNMS at 50% or higher threshold).

In this study, the PNMS at 50% threshold was used to generate deterministic model choice regions to calculate Dice Similarity Coefficient between the two techniques. Choosing different thresholds would directly affect the extent of the three model regions generated by the PNMS technique. Our group has investigated[10] the information content and stability of different information modalities (raw signal intensity profiles: 1st and 2nd echoes) against different probability thresholds to estimate different model regions generated by the NMS technique. The results (high Silhouette coefficients) of the study revealed the robustness (the mean and standard deviation values of the Silhouette coefficients, SCs, for the two raw DCE-MR information were: 0.392 ± 0.162 and 0.332 ± 0.131, for the 1st and 2nd echoes, respectively) of the model-based clusters on the KSOM feature space and their associations with the physiological state (identified by the NMS analysis using three observation equations) of tissue in rat brain. As a future work, a similar study can be conducted for the ΔR_1 profiles (used in this study for PNMS technique) to reveal the robustness of the PNMS against different probability thresholds.

The k-fold NCV analysis performed in this study, reveals the information content of different model-based (ΔR_1) profiles and their stabilities to describe the three pathophysiological states of the tissue. As shown in Table 1, the average values of the permeability parameters reported for the outer loops of the k-fold NCV (k = 10) are less (the MPDs for the three permeability parameters were: -28%, +18%, and +24% for v_p, K^{trans}, and v_e, respectively) than the values estimated by the conventional NMS technique. Interestingly, the variations (all confident intervals) of the permeability parameters estimated by the K-SOM-PNMS are less than their values estimated by the conventional NMS technique.

The K-SOM is an unsupervised network. During the training phase, no annotated/labeled information is used to identify BMUs or number of hits for each of the neurons in the network topology. Thus, during the training phase, the K-SOM is not affected by any potential model misclassification generated by the conventional NMS. Once the network is trained, it is locked/frozen, and the model probability maps are built from its final hit map by tracing the hits back to their nested Models in the real domain, using their labels. Therefore, any misclassification or errors generated by the conventional NMS would affect the validation/testing phase of the study and would appear and be manifested on the feature space as penumbra effect or diffusion/overlap of the model clusters, affecting the performance of the validation/testing phase of the study.

The ΔR_1 profiles estimated in this study can be susceptible to noise, arterial input function dispersion or delay[33,34], contrast agent arrival time differences among different animals, etc. These systematic and random effects can result in uncertainties in the classification models, both conventional and probabilistic NMS techniques. For the other *known* sources of systematic error, a data-driven approach to model selection will minimize over- or under-fitting to these parameters[2,3]. Of note, if the data has systematic errors due to measurement, data-driven approaches will likely be limited.

It is clear from an examination of the data that there are elements in modeling DCE-MRI that are not accounted for (*cf. Figure 8 of Ewing and Bagher-Ebadian*[2]) and cannot be accounted for if over-fitting is to be avoided. These 'tapering effects' are typical in modeling of all biological systems[1]. As long as effects due to T2* dephasing are accounted-for in the acquisition, the two most evident sources of error are errors in estimating the true arterial contrast agent concentration, and dispersion due to flow of the arterial input function (AIF) as it progresses from the large arteries to the capillary bed, where exchange with the extravascular space takes place. Estimating the true AIF concentration presents significant difficulties, with inflow, outflow, and partial-volume effects undermining efforts at the site of measurement. This, and dispersion in the arterial tree[35,36] substantially undermine the assumption that either the amplitude or the shape of the tissue input function can be determined from a time trace of arterial contrast. One approach to estimating input amplitude is to employ a group-averaged time trace of arterial CA concentration normalized to a known vascular volume in normal brain tissue (putamen)[2,37], thus deliberately introducing a bias that is presumably smaller than the bias of measuring contrast change directly from a large artery and inferring dynamic contrast agent concentration. This does not address problems with AIF dispersion. Therefore, quantification of all these tapering effects and estimation of their impacts on the raw DCE-MRI signal and their propagations into the tissue response is very complex and hard to simulate for the validation of the NMS and K-SOM PNMS techniques. As future works, investigation of these systematic and random effects on the performances of the conventional and probabilistic NMS techniques is warranted.

Our group has studied[3] the sampling distribution of the generated F-test within the region of brain's normal tissue. We have shown that it is unlikely that the errors of the fit of any model (1, 2 and 3) to typical concentration-time data in tissue would be iid (independent and identically distributed) and normally distributed. It is also known a priori that contrast agent does not leak into normal brain tissue at any detectable rate during the course of DCE-MRI experiment, and therefore Model 1 must be true for the null hypothesis testing of NMS within the brain normal tissue. The nesting described is the only nesting that is physiologically reasonable.

For non-leaky tissues ($K^{trans} = 0$), there are a number of possible causes of the visible dispersion that occurs. There may in fact be some penetration of the blood-brain barrier by the CA; possibility for some small molecules penetrating the tissue of those vessels that are surrounded by smooth and normal muscles. There is undoubtedly some dispersion in the shape of the input function that is due to the branching of the vessels between the major arteries, where the AIF must be sampled, and the arterioles that deliver the CA to the capillary bed of the tissue. Additionally, there is dispersion in the capillary bed itself, and finally there is some restriction of water exchange between the intravascular plasma, where the CA resides, and the extravascular tissue, where the great majority of tissue water, and therefore the great majority of MRI signal, resides[2]. Thus, an inspection of the Model 1 time trace (see Ref[3]. , Fig. 2) demonstrates that, although there is no leakage in the tissue, dispersion in the intervening vasculature changes the shape of the input function. The model states that the shape of the AIF and tissue response will be kind of the same, but with amplitudes dependent on the vascular volume. This is clearly not the case. The combination of low contrast-to-noise, dispersion, and possibly limited transvascular water exchange, appear to have increased the sampling distribution of the F-test in tissue that is known not to have a leaky microvasculature.

The PNMS technique allows quantification of different uncertainty levels relevant to the three nested models in the conventional NMS analysis. Indeed, it offers probabilistic adjustments to the permeability parameters (see Eqs. 4–6) estimated by the conventional NMS for the voxels containing a combination of multiple models. The model probabilities/weights within each voxel estimated by the PNMS technique are associated with different tissue characteristics (different combinations of non-leaky tissue, leaky tissue with and without CA absorption with different ratios). We believe that the extreme values of these weights/probabilities could be potentially validated using rat brain's histology information. Our group has already investigated[2] different zones (such as rim of the tumor, presumably leaky) of the rat brain tumor, stained for von Willebrand factor (vessels) and counterstained with hematoxylin[38]. The results of the study confirm the probability maps around the tumor (mainly for model 2 region) generated by the PNMS analysis. As shown in the third column of Fig. 5, the brighter green color (corresponding to higher Model 2 probability/weight) around the rim of tumor could be associated with the tumor tissues that are highly vascularized (with high CA leakage and low CA absorption) that are surrounded with normal tissue that causes a high CA concentration gradient with low interstitial fluid pressure.

One of the first self-organizing algorithms[28], the K-SOM algorithm groups multi-dimensional data in the form of clusters on feature space with no supervision of the intent of visualization, clustering analysis, and dimensionality reduction[17–21,28,39]. Nonlinear dimensionality reduction, unsupervised learning, intuitive clustering relationship, feature space visualization, easy interpretation, flexibility to work with numerical, categorical, and discrete datasets as well as robustness to the noise of the signal are the most important benefits of using the K-SOMs[40]. Many improvements[28,39] have been proposed to the original architecture, which include the Batch-SOM[28], Dot-Product-SOM[28], a SOM that focuses on identifying a linear combination of model vectors instead of winner nodes[29]. For instance, the $O(\log_2 M)$-SOM[41] utilizes a stratification technique that inherently deals with propagation to neighborhood nodes on the feature space. The main goal of these evolved versions of the K-SOM is to prioritize and improve the optimization and representation of feature information within the feature space. Other algorithms that can also improve the original K-SOM's performance, stability, convergence, and its adaptability with other problems include Growing Grid SOM[42], Growing Neural Gas[43] algorithms, and Hierarchical-SOM[44]. These algorithms consist of an additional layer of nodes to automatically determine the optimal topology size of the K-SOM based on the properties and cost functions determined by the original algorithm. Despite the promising advantages provided by these modified K-SOM algorithms over its original version such as memory and speed optimizations, as well as improved data representation, they may be susceptible to bias in generating clusters and in the quality of the feature visualization on the feature space. In this study, the K-SOM's topology size was selected as 8×8 that can produce a maximum of 64 distinctive clusters on the image space. Choosing a larger size of the K-SOM's topology would increase the precision of the estimated probabilities for different models. However, as the size of the network increases, the chance of the network running into an over-fitting condition and capturing more detailed information that could be irrelevant to the meaningful spatiotemporal trend of the pathophysiological state of the tissue increases. Thus, further investigation of the effects of different K-SOM's architecture, topology sizes, the recruited algorithms, its comparison with different unsupervised models such as AutoEncoders[45,46], as well as other model averaging techniques such as Akaike's Information Criteria (AIC)[13,47], AIC corrected (AICc), Bayesian information criteria (BIC)[48,49] and their impact on the model efficiency for probabilistic NMS analysis of DCE-MRI data is warranted[13,50].

Indeed, different scan times would affect the evolution of models during the course of the experiment, and model regions would approach an equilibrium condition differently over the duration of the study. Our group has previously studied[51,52] the effect of different scan times on the evolution of the three models during the course of DCE-MR experiment. We have shown[51,52] that the Model Evolution (ME) profiles in the course of DCE-MRI experiment, depend highly on the inward/outward intravoxel diffusion of contrast agent and contain abundant information for describing the compartmentalization and heterogeneity levels of solid tumors. Therefore, different K-SOMs should be developed for the PNMS analysis for different scan time.

This study demonstrates an application of an adaptive unsupervised model to improve robustness and computation speed of the NMS technique that appear in conventional approaches to estimate DCE-MRI vascular parameters. Compared to conventional NMS methods, the trained K-SOM PNMS technique is computationally faster and takes a fraction of a second (Core (TM)-6700HQ, CPU @2.60 Hz) to calculate all the probabilistic NMS maps for an entire 3D DCE-MRI brain volume (for entire animal brain with 3 full slices). The conventional NMS analysis assigns one of the three nested models to each voxel prior to the estimation of its permeability parameters, PK analysis. The K-SOM PNMS analysis assigns three probabilities (associated with

the three models) to each voxel prior to its final PK analysis. Indeed, the final PK analysis is performed following the estimation of the model labels (for the conventional NMS) or the model probabilities (for the PNMS). The trained K-SOM provides the probability estimates of the three models in a fraction of second, while it would take longer for the conventional NMS to estimate the model choice map for the same dataset. Thus, the K-SOM performs the probabilistic version of the NMS along with uncertainty analysis much faster than the conventional NMS. However, in order to estimate the probabilistic permeability parameters (Eqs. 4–6), without applying any specific threshold, the speed of the proposed PNMS would be comparable with the conventional NMS.

Conclusions

This work establishes an important first step toward spatiotemporal MR characterization of brain and brain tumor regions using a probabilistic nested model selection technique. This is fundamental toward an accurate estimation of vasculature parameters critical in staging tumors, evaluating early tumor response to treatments, as well as designing and optimizing DCE-MR imaging for precise characterization of brain tumors.

Data availability

All imaging data used in this investigation along with programming codes and results are available and can be shared upon reasonable request to Drs. Hassan Bagher-Ebadian, Stephen Brown, and James R. Ewing.

References

1. Burnham, K. P. & Anderson, D. R. *Model Selection and Multimodel Inference: A Practical Information-Theoretic Approach* (second edn, (Springer, 2002).
2. Ewing, J. R. & Bagher-Ebadian, H. Model selection in measures of vascular parameters using dynamic contrast-enhanced MRI: experimental and clinical applications. *NMR Biomed.* **26**, 1028–1041. https://doi.org/10.1002/nbm.2996 (2013).
3. Bagher-Ebadian, H. et al. Model selection for DCE-T1 studies in glioblastoma. *Magn. Reson. Med.* **68**, 241–251. https://doi.org/10.1002/mrm.23211 (2012).
4. Valadie, O. G. et al. Characterization of the Response of 9L and U-251 N Orthotopic Brain Tumors to 3D Conformal Radiation Therapy. *Radiat. Res.* **199**, 217–228. https://doi.org/10.1667/RADE-22-00048.1 (2023).
5. Paudyal, R., Bagher-Ebadian, H., Nagaraja, T. N., Fenstermacher, J. D. & Ewing, J. R. Modeling of Look-Locker estimates of the magnetic resonance imaging estimate of longitudinal relaxation rate in tissue after contrast administration. *Magn. Reson. Med.* **66**, 1432–1444. https://doi.org/10.1002/mrm.22852 (2011).
6. Elmghirbi, R. et al. Toward a noninvasive estimate of interstitial fluid pressure by dynamic contrast-enhanced MRI in a rat model of cerebral tumor. *Magn. Reson. Med.* **80**, 2040–2052. https://doi.org/10.1002/mrm.27163 (2018).
7. Kilkenny, C. et al. Animal research: reporting in vivo experiments: the ARRIVE guidelines. *J. Gene Med.* **12**, 561–563. https://doi.org/10.1002/jgm.1473 (2010).
8. Leung, V., Rousseau-Blass, F., Beauchamp, G. & Pang, D. S. J. ARRIVE has not ARRIVEd: Support for the ARRIVE (Animal Research: Reporting of in vivo Experiments) guidelines does not improve the reporting quality of papers in animal welfare, analgesia or anesthesia. *PLoS One.* **13**, e0197882. https://doi.org/10.1371/journal.pone.0197882 (2018).
9. Rice, A. S. C. et al. Transparency in the reporting of in vivo pre-clinical pain research: The relevance and implications of the ARRIVE (Animal Research: Reporting In Vivo Experiments) guidelines. *Scand. J. Pain.* **4**, 58–62. https://doi.org/10.1016/j.sjpain.2013.02.002 (2013).
10. Bagher-Ebadian, H. et al. Radiomics characterization of tissues in an animal brain tumor model imaged using dynamic contrast enhanced (DCE) MRI. *Sci. Rep.* **13**, 10693. https://doi.org/10.1038/s41598-023-37723-8 (2023).
11. Bagher-Ebadian, H. et al. Dynamic contrast enhanced (DCE) MRI estimation of vascular parameters using knowledge-based adaptive models. *Sci. Rep.* **13**, 9672. https://doi.org/10.1038/s41598-023-36483-9 (2023).
12. Brix, G., Schad, L., Deimling, M. & Lorenz, M. Fast and precise T1 imaging using a TOMROP sequence. *Magn. Reson. Imaging.* **8**, 351–356. https://doi.org/10.1016/0730-725x(90)90041-y (1990).
13. Brix, G., Zwick, S., Kiessling, F. & Griebel, J. Pharmacokinetic analysis of tissue microcirculation using nested models: multimodel inference and parameter identifiability. *Med. Phys.* **36**, 2923–2933. https://doi.org/10.1118/1.3147145 (2009).
14. Patlak, C. S., Blasberg, R. G. & Fenstermacher, J. D. Graphical evaluation of blood-to-brain transfer constants from multiple-time uptake data. *J. Cereb. Blood Flow. Metab.* **3**, 1–7 (1983).
15. Patlak, C. & Blasberg, R. Graphical Evaluation of blood to brain transfer constants from multiple time up take data. Generalizations. *J. Cereb. Blood Flow. Metab.* **5**, 584–590 (1985).
16. Nagaraja, T. N. et al. The MRI-measured arterial input function resulting from a bolus injection of Gd-DTPA in a rat model of stroke slightly underestimates that of Gd-[14 C]DTPA and marginally overestimates the blood-to-brain influx rate constant determined by Patlak plots. *Magn. Reson. Med.* **63**, 1502–1509. https://doi.org/10.1002/mrm.22339 (2010).
17. Lim, S. P. & Haron, H. Cube Kohonen self-organizing map (CKSOM) model with new equations in organizing unstructured data. *IEEE Trans. Neural Netw. Learn. Syst.* **24**, 1414–1424. https://doi.org/10.1109/TNNLS.2013.2259259 (2013).
18. Zampighi, L. M., Kavanau, C. L. & Zampighi, G. A. The Kohonen self-organizing map: a tool for the clustering and alignment of single particles imaged using random conical tilt. *J. Struct. Biol.* **146**, 368–380. https://doi.org/10.1016/j.jsb.2004.01.008 (2004).
19. Hathaway, R. J., Bezdek, J. C. & Pal, N. R. Sequential Competitive Learning and the Fuzzy c-Means Clustering Algorithms. *Neural Netw.* **9**, 787–796. https://doi.org/10.1016/0893-6080(95)00094-1 (1996).
20. Kia, S. J. & Coghill, G. G. Unsupervised clustering and centroid estimation using dynamic competitive learning. *Biol. Cybern.* **67**, 433–443. https://doi.org/10.1007/BF00200987 (1992).
21. Rumelhart, D. E. M. & James, L. *Parallel distributed processing: explorations in the microstructure of cognition* Vol. 2 (Cambridge, Mass.: MIT Press,, 1986).
22. Sørensen, T. A method of establishing groups of equal amplitude in plant sociology based on similarity of species and its application to analyses of the vegetation on Danish commons. *Kongelige Danske Videnskabernes Selskab.* **5**, 1–34 (1948).
23. Cawley, G. C. & a., T. On over-fitting in model selection and subsequent selection bias in performance evaluation. *J. Mach. Learn. Res.* **11**, 2079–2107 (2010).
24. Steyerberg, E. W. & Harrell, F. E. Jr. Prediction models need appropriate internal, internal-external, and external validation. *J. Clin. Epidemiol.* **69**, 245–247. https://doi.org/10.1016/j.jclinepi.2015.04.005 (2016).
25. Collins, G. S., Reitsma, J. B., Altman, D. G. & Moons, K. G. Transparent Reporting of a multivariable prediction model for Individual Prognosis Or Diagnosis (TRIPOD). *Ann. Intern. Med.* **162**, 735–736. https://doi.org/10.7326/L15-5093-2 (2015).

26. Spencer, R. G., Ferretti, H. A. & Weiss, J. A. Spillover and Incomplete Saturation in Kinetic Measurements. *J. Magn. Reson.* **101**, 294–296 (1993).
27. Paudyal, R., Nagaraja, B. E. H., Panda, T. N., Fenstermacher, S. & Ewing, J. D. JR,. MRI Look-Locker Estimates of the Longitudinal Relaxation Rate Are Approximately Linear in Contrast Agent Tissue Concentration. *Int. Soc. Magn. Reson. Med.* 1 (2008).
28. Kohonen, T. *Self-Organizing Maps* 2nd edn (Edition edn, Springer, 1997).
29. Kohonen, T. Description of Input Patterns by Linear Mixtures of SOM Models. *Helsinki Univ. Technol. Adapt. Inf. Res. Centre* **1** (2007).
30. Jacobs, V. L., Valdes, P. A., Hickey, W. F. & De Leo, J. A. Current review of in vivo GBM rodent models: emphasis on the CNS-1 tumour model. *ASN Neuro.* **3**, e00063. https://doi.org/10.1042/AN20110014 (2011).
31. Radaelli, E. et al. Immunohistopathological and neuroimaging characterization of murine orthotopic xenograft models of glioblastoma multiforme recapitulating the most salient features of human disease. *Histol. Histopathol.* **24**, 879–891. https://doi.org/10.14670/HH-24.879 (2009).
32. Candolfi, M. et al. Intracranial glioblastoma models in preclinical neuro-oncology: neuropathological characterization and tumor progression. *J. Neurooncol.* **85**, 133–148. https://doi.org/10.1007/s11060-007-9400-9 (2007).
33. Nejad-Davarani, S. P. et al. An extended vascular model for less biased estimation of permeability parameters in DCE-T1 images. *NMR Biomed.* **30** https://doi.org/10.1002/nbm.3698 (2017).
34. Liberman, G. et al. DUSTER: dynamic contrast enhance up-sampled temporal resolution analysis method. *Magn. Reson. Imaging.* **34**, 442–450. https://doi.org/10.1016/j.mri.2015.12.014 (2016).
35. Nejad-Davarani, S. P. et al. An extended vascular model for less biased estimation of permeability parameters in DCE-T1 images. *NMR Biomed.* **30** (2017).
36. Nejad-Davarani, S. P. et al. A parametric model of the brain vascular system for estimation of the arterial input function (AIF) at the tissue level. *NMR Biomed.* **30** (2017).
37. Dehkordi, A. N. et al. DCE-MRI prediction of survival time for patients with glioblastoma multiforme: using an adaptive neuro-fuzzy-based model and nested model selection technique. *NMR Biomed.* (2017).
38. Chuang, S., Yung, Y. C. & von Li, C. Y. Willebrand Factor Is the Most Reliable Immunohistochemical Marker for Megakaryocytes of Myelodysplastic Syndrome and Chronic Myeloproliferative Disorders. *Am. J. Clin. Pathol.* **113**, 506–511 (2000).
39. Feyereisl, J. & Aickelin, U. Self-Organizing Maps In Computer Security. *arXiv preprint arXiv:1612.07003- arXiv.* https://doi.org/10.48550/ARXIV.1608.01668, doi: arXiv. (2016). https://doi.org/10.48550/ARXIV.1608.01668
40. Costa, L. E. B. & d., S. J. A. F. *Clustering, Noise Reduction and Visualization Using Features Extracted from the Self-Organizing Map*. Vol. 8206 242–251Heidelberg, (2013).
41. Kusumoto, H. & Takefuji, Y. O(log2M) Self-Organizing Map Algorithm Without Learning of Neighborhood Vectors. *IEEE Trans. Neural Networks.* **17**, 1656–1661. https://doi.org/10.1109/TNN.2006.882370 (2006).
42. Fritzke, B. Growing Self-organizing Networks - Why? *ESANN'96: Eur. Symp. Artifcial Neural Networks.* **1**, 61–72 (1996).
43. Fritzke, B. A growing neural gas network learns topologies. *Inform. Process. Systems-Advances Neural Networks- MIT Press.* **7**, 625–632 (1995).
44. Kayacik, G. H., Zincir-Heywood, N. A. & Heywood, M. I. On the Capability of an SOM Based Intrusion Detection System. *Proc. Int. Joint Conf. Neural Networks.* **3**, 1808–1813 (2003).
45. Kramer, M. A. Nonlinear principal component analysis using autoassociative neural networks. *AIChE J.* **37**, 233–243. https://doi.org/10.1002/aic.690370209 (1991).
46. Kramer, M. A. Autoassociative neural networks. *Computers & Chemical Engineering-Neutral network. Appl. Chem. Eng.* **16**, 313–328. https://doi.org/10.1016/0098-1354(92)80051-A (1992).
47. Bozdogan, H. Model selection and Akaike's Information Criterion (AIC): The general theory and its analytical extensions. *Psychometrika* **52**, 345–370. https://doi.org/10.1007/BF02294361 (1987).
48. Bollen, K. A., Harden, J. J., Ray, S. & Zavisca, J. BIC and Alternative Bayesian Information Criteria in the Selection of Structural Equation Models. *Struct. Equ Model.* **21**, 1–19. https://doi.org/10.1080/10705511.2014.856691 (2014).
49. Mohammad-Djafari, A. & Regularization Bayesian Inference, and Machine Learning Methods for Inverse Problems. *Entropy (Basel).* **23** https://doi.org/10.3390/e23121673 (2021).
50. Bagher-Ebadian, H. et al. MR Estimation of Permeability Parameters in Dynamic Contrast Enhanced Studies Using Model Averaging Technique and Nested Model Selection Method. *Proc. Intl. Soc. Mag. Reson. Med. 22* (Milan, Italy 1, 4090 (2014). (2014).
51. Bagher Ebadian, H. et al. Model evolution technique as a novel concept for characterization of tumor heterogeneity in dynamic contrast enhanced MRI studies. *Bioinformatics and Systems Biology, The American Association for Cancer Research (AACR)- 107th Annual Meeting* April 16–20 in New Orleans, USA 76, doi: (2016). https://doi.org/10.1158/1538-7445.AM2016-2710 Published July 2016 (2016).
52. Bagher-Ebadian, H. et al. Model Evolution Concept in Dynamic Contrast Enhanced MRI for Prediction of Tumor Interstitial Fluid Pressure. *Neuro-Oncology2015 / 11 Vol. 17; Iss. suppl 5* 17, doi: (2015). https://doi.org/10.1093/neuonc/nov236.5

Acknowledgements

Author contributions

Conceptualization, methodology, investigation, modeling, validation, and manuscript writing were performed by H.B.E., K.T., and J.R.E — Review and scientific editing were performed by H.B.E., K.T., S.L.B., I.J.C, and M.M.G. — MR Data acquisition and conventional pharmacokinetic modeling of DCE-MRI data were performed by J.R.E., H.B.E., S.L.B., and P.C.A. —Data curation, pre-processing, and data inspection were performed by H.B.E, K.T, J.R.E. and M.M.G.— Resources and Supervision: H.B.E., K.T, B.M., J.R.E., S.L.B., and I.J.C. — Project administration, funding acquisition: H.B.E., K.T, B.M., S.L.B., and J.R.E.

Declarations

Competing interests

The authors declare no competing interests.

Animal study

This study was approved at the Institutional Animal Care and Use Committee (IACUC) board of Henry Ford Health System and conducted with an approved IACUC # 1509. The animal study of this work was performed

and reported in compliance with the ARRIVE guidelines.

Additional information

Supplementary Information The online version contains supplementary material available at https://doi.org/10.1038/s41598-024-83306-6.

Correspondence and requests for materials should be addressed to H.B.-E.

Reprints and permissions information is available at www.nature.com/reprints.

Publisher's note Springer Nature remains neutral with regard to jurisdictional claims in published maps and institutional affiliations.